Influence of Spike Geometry on Electromagnetic Field Enhancement and the Linear and Nonlinear Plasmonic Properties of Gold Nanourchins

Domantas Peckus[1,2*], Fatima Albatoul Kasabji[3,4], Maziar Moussavi[1], Loic Vidal[3,4], Hana Boubaker[3,4], Asta Tamulevičienė[1,2], Arnaud Spangenberg[3,4], Tomas Tamulevičius[1,2], Joel Henzie[5*], Karine Mougin[3,4*], Sigitas Tamulevičius[1,2*]

[1]Institute of Materials Science of Kaunas University of Technology, K. Baršausko st. 59, LT-51423, Kaunas, Lithuania

[2]Department of Physics, Kaunas University of Technology, Studentų st. 50, LT-51368, Kaunas, Lithuania

[3]Institut de Science des Matériaux de Mulhouse IS2M UMR 7361, 15 rue Jean Starcky, F 68100 Mulhouse, France

[4]Université de Strasbourg, 4 Rue Blaise Pascal, CS 90032, F-67081 Strasbourg, France

[5]International Center for Materials Nanoarchitectonics (WPI-MANA), National Institute for Materials Science (NIMS), Tsukuba, Ibaraki 305-0044, Japan

*Corresponding authors

D. Peckus: domantas.peckus@ktu.lt, orcid.org/0000-0002-4224-2521;

J. Henzie: henzie.joeladam@nims.go.jp, orcid.org/0000-0002-9190-2645;

K. Mougin: karine.mougin@uha.fr, orcid.org/0000-0002-0481-1594;

S. Tamulevičius: sigitas.tamulevicius@ktu.lt, orcid.org/0000-0002-9965-2724.

Abstract

Wet-chemistry synthesized Gold nanourchins (Au NUs), characterized by spiky morphologies with spherical cores, exhibit complex and geometry-dependent plasmonic field enhancement properties distinct from those of symmetrical nanostructures. While plasmon hybridization and mode coupling in branched nanostructures have been broadly studied, the specific optical behavior of Au NUs—particularly regarding spike length distribution and ultrafast dynamics—remains underexplored. This study investigates the steady-state and transient absorption spectra of Au NUs with 50–80 nm cores and 5–20 nm spikes, revealing multiple resonance bands. Transient absorption spectroscopy at various excitation wavelengths confirmed the presence of distinct resonances. Electromagnetic simulations based on TEM tomography-inspired models identified two key extinction bands: a green-wavelength dark mode resonance and a red/nIR spike-induced resonance attributed to the lightning rod effect. Simulations further showed that short, uniformly distributed spikes (aspect ratio ≤ 1) weakly excite dark resonances, while longer spikes (aspect ratio > 1) induce hybridized longitudinal resonances and significant redshifts. Broad spike length distributions result in multiple coexisting resonances, aligning with experimental extinction spectra. A preliminary surface-

enhanced Raman scattering study using 2-naphthalene thiol confirmed stronger enhancement for long-spiked Au NUs under 785 nm excitation, validating the field enhancement potential of the identified resonances.

Keywords: Au nanourchins, spikes of Au nanourchins, localized surface plasmon resonance, transient absorption spectroscopy, EM modeling

Introduction

Plasmonic metallic nanoparticles and nanostructures are interesting due to their optoelectronic properties. Leveraging their size and shape-dependent localized surface plasmon resonance (LSPR) properties, nanostructures can be used for photocatalysis, nonlinear optics, [2] surface-enhanced Raman spectroscopy (SERS), [3] enhanced fluorescence, [4] sensors, [5] photovoltaics, [6] biosensors, [7] medicine, [8,9] authentication keys, [10] and soft 3D nanoporous structures. [11] Selecting the most suitable plasmonic material for a given nanostructure application necessitates consideration of factors such as the metal type, [12] nanostructure size, [13] shape, [13] and crystallinity. [14] So far, the most popular metals for plasmonic applications are Au and Ag. Various forms of Au nanostructures can be synthesized, resulting in symmetrical forms like spheres, cubes, tetrahedra, and nanorods [13] or nonsymmetrical - like nanourchins, [15,16] nanostars, [4,17,18] and nanoflowers. [19] These nonsymmetrical nanostructures can look quite similar; therefore, sometimes these names are used as synonyms, [8] because both have core and spikes, but there are some characteristic differences too. Nanourchins have a spiky, spherical shape, similar to sea urchins, with many protrusive, sharp tips. Their surface is usually covered with small, uneven length and thickness spikes. [20,21] On the other hand, nanostars have a star-shaped morphology with a central core and several sharp, well-defined, elongated tips extending outwards. [22–24] While instead of spikes, Au nanoflowers have petals attached to the core. [25,26]

The optical properties of symmetric Au nanoparticles are well described by Mie scattering theory, whereas the properties of asymmetric Au nanoparticles are less thoroughly explored, despite their potential for higher efficiency in specific applications such as medicine, biosensing, *in vivo* imaging, drug delivery, photothermal therapy, and photodynamic therapy. [8] Au nanostars, a counterpart of Au nanourchins (Au NUs), have already proven to be very efficient for SERS. [22] It has been demonstrated that Au NUs offer advantages over Au nanospheres or Au nanorods in SERS measurements. [7,15,20] Currently, more scientific research on optical properties is being conducted on Au nanostars compared to Au NUs, [27,28] but both of them seem to be promising for future plasmonic applications.

Various wet-chemistry methods exist for the synthesis of Au NUs, but they can generally be classified into seeded or seedless growth approaches. Among these, the seed-mediated method, where silver nanoparticles serve as silver seeds, is the most employed for preparing Au NUs. By separating the nucleation and growth processes, this method provides better control over the final size and morphology of Au NUs. Factors such as solution pH, temperature, seed quantity, size, composition, and other variables can be adjusted to achieve the desired characteristics. [29] Silver seeds used to prepare Au NUs were successfully synthesized by F.G. Xu *et al.* using a seed-mediated method, which is quite facile and does not need any template or surfactant agent. [30] N.G. Bastús *et al.* showed the possibility of synthesizing highly monodisperse and long-term stable and functionalizable Ag NPs. [31,32]

NPs results in various shape and high-resolution transmission electron microscopy (HR-TEM) or scanning electron microscopy (SEM) [33] is usually the first choice for inspection. On the other hand, the preparation of a sample for measurements takes a lot of time, and a limited number of nanoparticles are usually investigated in comparison to optical methods. [34]

One of the most used indirect ways to determine the size, shape, and homogeneity of plasmonic metal nanoparticles is steady-state UV-Vis-nIR absorption measurements, [16,34,35] where different geometrical form factors influence the light scattering and absorption properties of nanoparticles, resulting in different LSPRs. Machine learning-based methods for interpreting extinction spectra are emerging. [36] The rigorous numerical methods help to extend the understanding of the LSPRs in the optical extinction spectra of more complex nanostructure geometries than spheres and ellipsoids. [36] However, steady-state optical spectra can still hinder some hard-to-deconvolute information due to the overlapping resonances. In contrast, the transient absorption ultrafast optical measurements can reveal additional important information, revealing resonances hindered by the dominating ones, especially about more complicated nanostructures. [13] It was shown that transient absorption spectroscopy (TAS) provided more details about the shape of nanoparticles in comparison to steady-state absorption spectra, which is limited to the analysis of Mie resonance decomposition. [13] The auxiliary information on the LSPR decay dynamics, TAS spectral composition of ground state bleaching can be very advantageous for the analysis of asymmetric Au nanostructures that were not systematically studied with TAS yet. TAS can provide information about the different LSPR species that are too weak to be observed with steady-state spectroscopy, as it was shown in. [13] Recent ultrafast plasmonic property studies with TAS span over variously shaped Au nanoparticles, [13] including spheres, [13] nanorods, [13,37] and nanoporous materials. [38,39]

Despite growing interest in nanourchins resulting in 82 hits in Web of Knowledge, of which 46 are about Au nanostructures, their optical properties are undeservedly still not explained in detail. The complex hybridized resonances in Au NUs are known to be composed of and influenced by the spherical core and random length and density nanospikes/nanorods, which were analyzed separately. [13] Likewise, a comprehensive TAS analysis of Au NUs has not been conducted yet. A deeper understanding of the electric field enhancement effects, broadly tailorable resonances and ultrafast properties of LSPR in Au NUs could significantly reinforce their utility across diverse applications in photonics. Therefore, we devoted this work to the first deep analysis of steady state and dynamic plasmonic optical properties of Au NUs. The proposed approach could be extended for Au nanostars and Au nanoflowers.

In this work, we have synthesized a set of Au NUs with different core sizes (50-80 nm) and spike lengths (6-15 nm) along with spherical Au nanoparticles of the same size. The conducted TEM imaging and tomography studies inspired the use of electromagnetic (EM) simulations and helped to explain the nature of the emerging broad extinction in the optical spectrum. Two different plasmonic bands in Au NUs with long spikes were observed not met for the short ones and explained the significance of the higher aspect ratio spikes hindered in the steady state extinction spectroscopy. The SERS measurements confirmed the importance of the electric field concentration in the longer spike nanourchins met in the numerical models.

Experimental section

Chemical Synthesis

Materials

Chemicals. Tannic acid (TA) ($C_{76}H_{52}O_{46}$), silver nitrate ($AgNO_3$), trisodium citrate ($Na_3C_6H_5O_7$), chloroauric acid ($HAuCl_4$), polyvinylpyrrolidone (PVP 40), and L-3,4-dihydroxyphenylalanine (L-DOPA), trisodium citrate dihydrate ($C_6H_5Na_3O_7 \cdot 2H_2O$) were purchased from Sigma-Aldrich. Ultrapure water (ρ = 18.2 MΩ·cm) was used in all experiments. Glassware was rinsed before use with aqua regia and then with pure water.

Synthesis of Gold Nanospheres

Synthesis of Au nanospheres (Au NSs) for imitating the core of the nanourchins was performed according to the route described in [40]. In short, the synthesis consists of two steps, starting from seed synthesis and further growth of nanoparticles. Seeds were synthesized by heating 150 ml of 2.2 mM sodium citrate solution for 15 min under vigorous stirring. After the solution started to boil, 1 ml of $HAuCl_4$ (25 mM) was injected. The color of the solution changed to soft pink in 10 min. Immediately after the seed synthesis, the reaction was cooled to 90°C, and 1 ml of $HAuCl_4$ (25 mM) was injected. The solution was left for 30 minutes stirring and heating at 90°C. These injection and stirring procedures were repeated two additional times. After that, 55 ml of the sample was extracted and added to the same vessel, 53 ml of water and 2 ml of 60 mM sodium citrate were added. This solution was then used as a seed solution for further growth. Repeating this sequence 4–6 times resulted in final nanoparticle diameters of 50–80 nm, respectively.

Synthesis of Silver Seeds

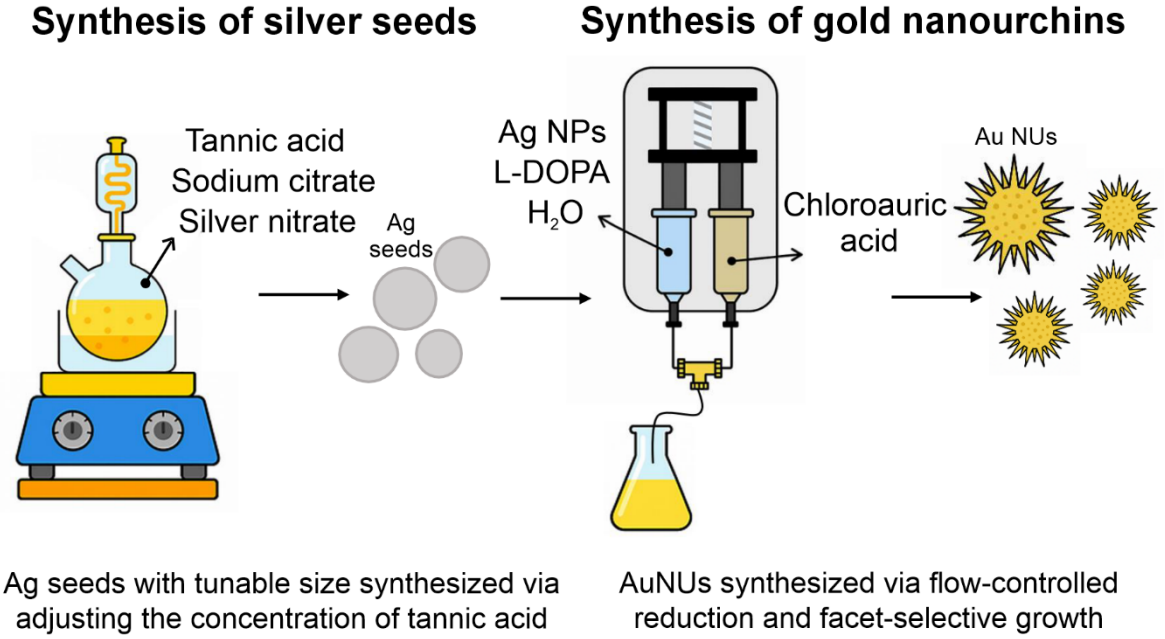
The silver nanoseeds were prepared according to the typical method reported by N.G. Bastús *et al.* They presented a method to synthesize a highly monodisperse sodium citrate-coated spherical silver nanoparticles (Ag NPs) by following a kinetically controlled seeded-growth approach via the reduction of silver nitrate by the combination of two chemical reducing agents: sodium citrate and tannic acid [31]. By adjusting the tannic acid concentration from 0.25 mM to 1 mM, the size of Ag NPs increased from 21.4 ± 5.0 nm to 37 ± 6.2 nm, respectively. The prepared silver seeds were used in the next section for the synthesis of Au NUs.

Synthesis of Au Nanourchins

The synthesis of Au NUs, was performed according to the formula proposed by A. Silvestri *et al.* [41]. Two solutions were prepared, solution "A", which is a mix of as-prepared silver seeds solution (see section 2.1.3), L-DOPA (12 mM) and ultrapure water with a 1:1:2.9 ratio, while solution "B" is $HAuCl_4$ solution (12 mM). The synthesis was carried out in a 'T'-shaped Mixer using two syringe pumps (**Figure S1**).

The microfluidic system depicted in **Scheme 1** was used to allow better mixing of the product and ensure homogeneity in the distribution of the NU's size. The core size was controlled by varying the concentration of tannic acid during the synthesis of the silver seeds, while the spike length was influenced by the timing of PVP addition during the synthesis of the nanourchins. More details are provided in the supporting information "Chemical synthesis" section (**Figure S2**).

Scheme 1. Synthesis scheme for originating controlled diameter Ag seeds for further growth of Au shells and spikes resulting in controlled spike length Au nanourchins.



A monolayer of gold nanoparticles was deposited on silicon according to the method described in [42]. 8 ml of colloidal solution (Au NSs or Au NUs) was diluted with 2 ml of deionized water in a glass beaker. Then, 8 ml of hexane was added dropwise on the surface of the solution. It forms an incompatible oil – water interface. At the end, 10 ml of ethanol is added slowly to the aqueous solution. The layer of NPs starts to assemble at the interface between the colloid-ethanol and hexane interface. After hexane evaporates, the monolayer is transferred on silicon.

Characterization

Transmission electron microscopy (TEM)

A drop of nanoparticles was dried on a carbon film grid and the micrographs were acquired with a high-resolution transmission electron microscope (HR-TEM) ARM200 (JEOL) equipped with a cold field emission gun (FEG) and used an acceleration voltage of 200 kV. Imaging using a rotating sample holder helped to determine the characteristic linear dimensions and size distributions of Au NUs and Au NSs. To achieve a three-dimensional visualization of the spikey particles, the nanourchins were imaged using TEM by tilting them from -50° to +60° in 1° increments, resulting in a total of 111 micrographs. These images were processed using a custom Python script, which employs the Local Feature Transformer (LoFTR) feature-matching algorithm [43] to align consecutive frames and correct for translational and rotational displacements. Dimensions of the NPs were measured with ImageJ software.

UV-Visible Spectroscopy

UV-Visible-near Infrared extinction spectra of the nanostructures under study were recorded using a fiber-optic spectrometer, AvaSpec-2048 (Avantes), with a resolution of 1.4 nm within the 200-1100 nm spectral range and utilizing a combined Deuterium Halogen light source, AvaLight-DHc (Avantes).

Transient absorption spectroscopy

Ultrafast relaxation processes in Au NPs (nanourchins, nanospheres) were investigated using a transient absorption spectrometer, HARPIA (Light Conversion). The system was excited with an ultrafast 290 fs pulse length and 1030 nm wavelength Yb:KGW laser Pharos (Light Conversion), with a regenerative amplifier at a 66.7 kHz repetition rate. The pump beam wavelength, based on the LSPR absorption maxima of the investigated NPs, was tuned to 350, 500, 600, 700, 750, and 800 nm using a collinear optical parametric generator, Orpheus, and a harmonic generator, Lyra (Light Conversion). The samples were subsequently probed with a white light supercontinuum generated using a 2 mm thickness sapphire plate excited with a fundamental laser wavelength (1030 nm). The spectral range of the supercontinuum probe, as well as the detection range of the TAS dynamics, spanned wavelengths from 480 to 783 nm. The excitation beam was focused on the 1 mm optical path length quartz cuvette (Hellma Analytics) to an approximately 700 μm diameter spot, overlaid with the supercontinuum probe, which was approximately 500 μm in diameter. The volume of the Au nanoparticle sample in water analyzed by TAS was approximately 2×10^{-7} mm³.

SERS analysis

The Raman spectral data of representative nanosphere and nanourchin samples were acquired using a micro-Raman spectrometer inVia (Renishaw) equipped with a thermoelectrically cooled 2048-pixel CCD detector. Samples were excited with two lasers through a 50x/0.75 NA objective (Leica): 532 nm (excitation power was 0.36 mW, laser spot size ~1 mm, 2400 lines/mm diffraction grating) and 785 nm (excitation power was 0.136 mW, laser spot size ~2 mm, 1200 lines/mm diffraction grating). The signal was collected for 10 seconds. 2-Naphthalenethiol (2NT) of 10^{-4}M concentration was used for testing the signal enhancement. Monolayer samples were immersed in the analyte solution and kept for 1h, afterwards, the samples were taken out and washed with ethanol to remove the excessive amount of analyte from the surface. For analysis in liquid keeping the same analyte concentration (10^{-4}M), measurements were performed with 785 nm excitation using long working distance objective 50x/0.5 NA (Leica). The analytical enhancement factor was calculated by comparing the signal with the reference of the signal acquired using 10^{-2} M analyte concentration, see supporting information **Section: SERS measurements**, for more details.

Electromagnetic simulations

Full-field EM simulations were performed on Au nanoparticles to estimate their optical properties at a wavelength range of 400 to 1200 nanometers when suspended in a medium equivalent to water (n =1.333). Nanourchin (NU) particles described in **Table S1** and **Section: TEM image analysis** were used as inspiration to create morphological models that possess the most important structural features using a code developed in Matlab. The models were then imported into the EM simulation software Lumerical. NUs with no core were created by overlapping their core using a sphere with n = 1.333. The Au optical constants described in McPeak *et al.* [44] were used to model the optical response of all nanoparticles because it has good coverage from visible to near-infrared wavelengths. Each Au NU model was excited with a broadband total field scattered field source, then the scattered and absorbed light was recorded with frequency-domain power monitors enclosing the particles.

Results and Discussion

TEM image analysis

Aiming to understand the optical properties of complex Au nanostructures, representative spherical gold nanoparticle samples were used, resembling the core or the overall effective size of the Au NUs. The wet chemistry method synthesized Au NPs resulted in 52±5 nm, 63±6 nm, and 78±8 nm in diameter, as was obtained from the TEM micrographs (**Figure 1**). More complex Au nanostructures—nanourchins with varying core sizes and spike lengths—were synthesized using the seed-mediated wet-chemistry method with Ag seeds (**Figure 1, S3**). The synthesized nanostructure TEM micrograph analysis results are summarized in **Table 1** where samples are grouped based on their characteristic linear dimensions. The histograms showcasing the linear dimension distributions of spikes are depicted in **Figure S4**.

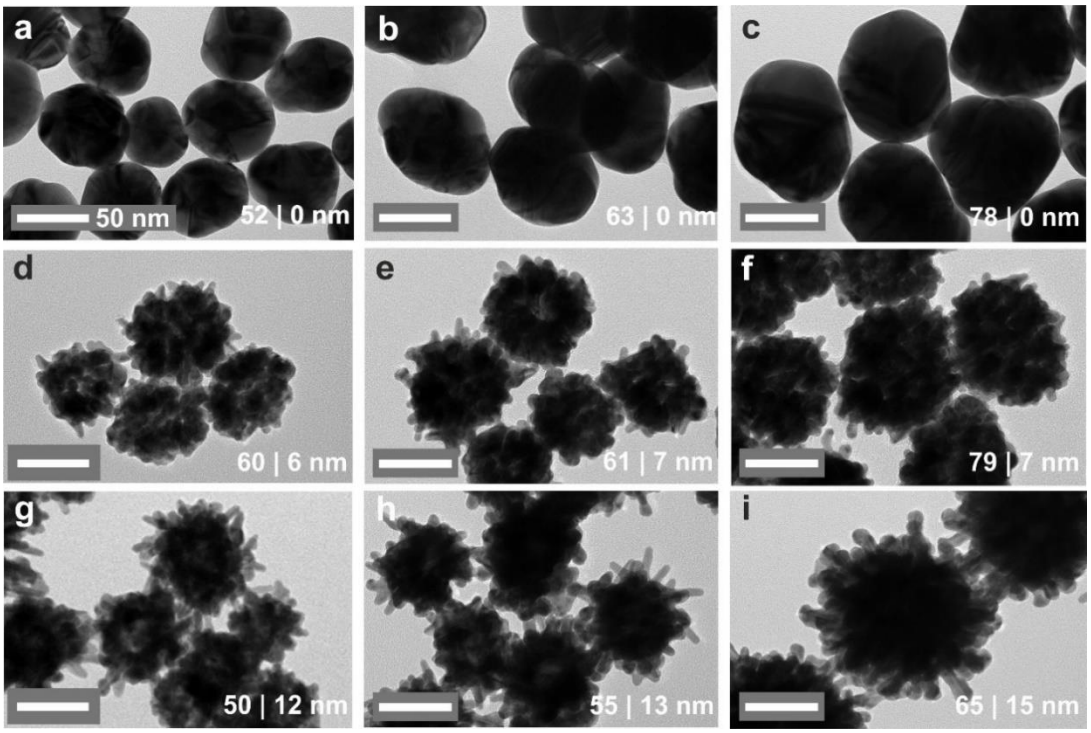


Figure 1. TEM images of Au nanospheres: Au NPs 52|0 nm (**a**); Au NPs 63|0 nm (**b**); Au NPs 78|0 nm (**c**) and Au nanourchins: Au NUs 60|6 nm (**d**); Au NUs 61|7 nm (**e**); Au NUs 79|7 nm (**f**); Au NUs 50|12 nm (**g**); Au NUs 55|13 nm (**h**) and Au NUs 65|15 nm (**i**). Three different groups of samples are in this figure first group **a**, **d**, **g**; the second **b**, **e**, **h** and the third **c**, **f**, **i**.

Table 1. Characteristic linear dimensions of Au nanosphere (NS) and Au nanourchins (NU). Their typical synthesis conditions, used Ag seed size, Au NS, and Au NU core diameters (D), spike lengths (L), and their aspect ratios (L/D) as obtained from **Figures 1, 3S**.

Sample		Comment on synthesis specifics	Linear dimensions (nm)			Spike Aspect Ratio
Name	NP type		Core|D	Spike|L	Spike|D	

52|0	Au NS	4 cycles: 53 ml of water and 2 ml of 60 mM sodium citrate, 25 mM $HAuCl_4$	51.5±4.7	-	-	-
63|0		5 cycles: 53 ml of water and 2 ml of 60 mM sodium citrate, 25 mM $HAuCl_4$	62.5±6.2	-	-	-
78|0		6 cycles: 53 ml of water and 2 ml of 60 mM sodium citrate, 25 mM $HAuCl_4$	77.5±7.9	-	-	-
60|6	Au NU	Small Ag seeds (22±4 nm) using 0.25 mM tannic acid with PVP in the gold solution	60.1±6.8	6.1±1.8	5.8±0.9	1.05
61|7		Medium Ag seeds (23.3±3.3 nm) using 1 mM tannic acid with PVP in the gold solution.	60.8±7.4	7.3±2.4	8.6±2.1	0.85
79|7		Large Ag seeds (27.1±4.1 nm) using 1 mM tannic acid with PVP in the gold solution	79.2±4.3	7.3±1.4	7.3±1.2	1.00
50|12		Small Ag seeds(22±4 nm) using 0.25 mM tannic acid	50±8.8	12±4.4	6.4±1.5	1.90
55|13		Medium Ag seeds(23.3±3.3 nm) using 1 mM tannic acid	55±6.8	13±3.9	7.6±1.9	1.70
65|15		Large Ag seeds(27.1±4.1 nm) using 1 mM tannic acid	64.8±16.9	15.3±5.4	10.1±1.8	1.50

A key challenge in characterizing Au NUs is determining the three-dimensional distribution of spike geometries from 2D TEM images. While TEM is essential for initial assessment, it is insufficient for a complete statistical analysis, as the micrographs are projections and the apparent spike lengths do not necessarily represent their true 3D lengths. To gain a better qualitative understanding of the 3D structure, a TEM tilt series was performed, rotating a sample from -50° to +60° to create a 3D visualization (**Video S1**, **Figure S5**). A full 3D reconstruction from these tilt series to find a precise distribution density is a goal for our future work.

Based on the data acquired from **Figure S5** and **Video S1** we made a digital twin of the Au NUs (**Figure S5**). Based on **Figure S5** the core is *ca.* 80±5 nm and spikes are 20±9 nm. We used 3 model types to show the influence of the spike distribution. The simplest one is the uniform model (**Figure 2**), where all spikes are of equal size. Unfortunately, it is a very simplified model and does not represent the randomness of the spikes, therefore, we created even more realistic models. For one of them, we used Sobol's sequence for spike length distribution [45,46]. It's designed to be homogeneous in distributing fluctuations, so the overall urchin shape has long and short spikes in every direction compared to the third investigated type - random spikes length distribution that can create asymmetric patterns (**Figure 2 b**). More details on the nanourchin models are provided in the supporting information. The asymmetric patterns can compensate one another for a very large population of samples like the ones we used for steady-state extinction spectroscopy or TAS measurements; therefore, the random sequence can be close to Sobol. The three proposed models with the spikes of 0 (nanosphere), 6, 12, and 20 nm (**Figure 2 b**) were used as an input for EM simulations.

Experimental optical properties

The UV-Vis-nIR absorbance spectra of synthesized nanospheres and nanourchins are compared in **Figure 2**. The LSPR-related extinction peaks for Au nanospheres and Au NUs look quite similar, but the peaks of Au NUs with long spikes are much broader (**Figure 2a**). The obtained Au NU absorption spectra are similar to the reported short-spike Au NUs. [20,47] The long spike Au NUs have much broader absorption extending into the near-infrared region. This broad absorption peak looks different from the reported ones for Au nanostars and nanoflowers with comparably long spikes, indicating two absorption peaks. [17,48]

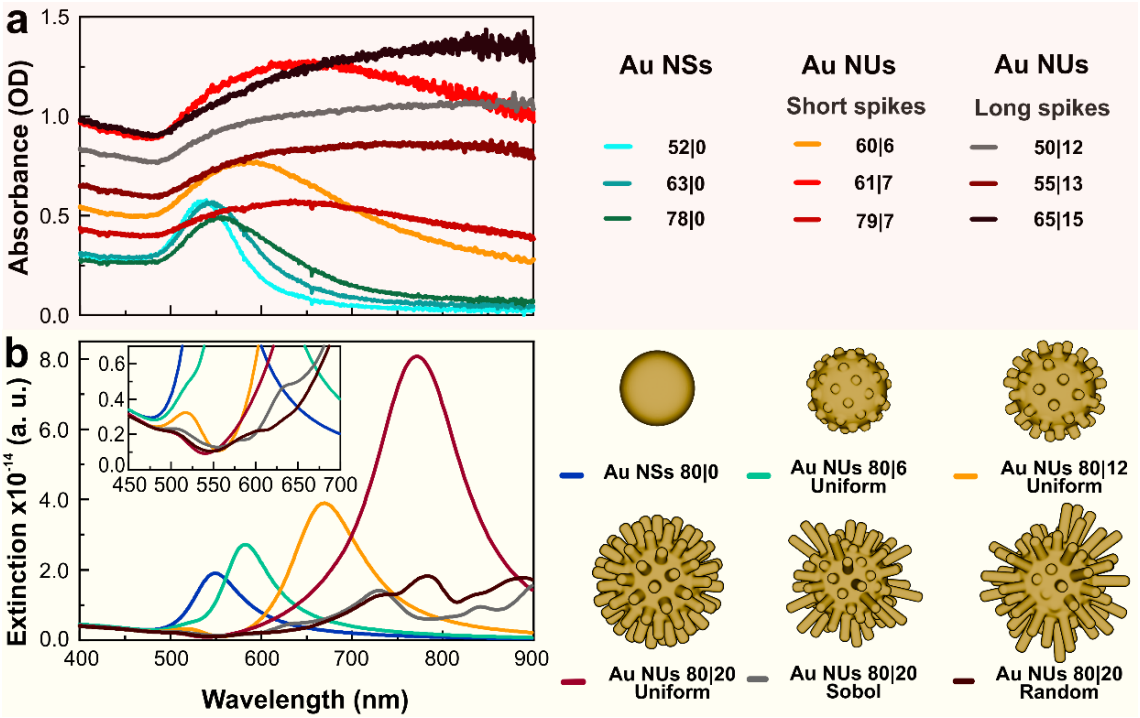


Figure 2. Experimental (**a**) and simulated (**b**) UV-Vis-nIR absorbance spectra of the analyzed Au spheres and nanourchins. The inset in (**b**) depicts the LSPR region related to the quadrupole of the sphere and transversal modes in the spikes. The legend of the modeling results depicts the 3D of the sphere of 80 nm diameter, uniform Au NUs of different spike lengths (6 nm, 12 nm, and 20 nm) with the same sized core, and two kinds of random Au NU models based on the TEM analysis (**Video S1**, **Figure S5**) Sobol (Sobol's sequences are a type of quasi-random low-discrepancy sequence) and random of the same average length spikes of 20 nm**.** The thickness of all spikes 10 nm.

Electromagnetic Simulation

To gain deeper insight into the optical properties of Au NUs and how their core and spikes influence the overall optical response, we developed a systematic EM simulation approach. Three kinds of 3D Au NU models – symmetrical (uniform), Sobol, and random, depicted in **Figure 2 b** were used, keeping the 80 nm core fixed and varying their spike lengths from 0 to 20 nm as explained in **Table S1**. Although the models were not perfectly accurate, even the representative approximate models of asymmetric nanoparticles can provide valuable information on how spike configuration changes sphere core optical and near-field distribution properties that help to explain the experimental UV-Vis-nIR absorbance spectra shown in **Figure 2 a**.

The EM simulations of a core without spikes (Au NS 80|0) resulted in a single LSPR dipole peak at 542 nm that matches the experimental UV-Vis-nIR extinction spectra and confirms the validity of the used Au dielectric function dispersions. The elongating spikes in the symmetrical spike distribution 3D model (**Figure 2 b**) resulted in the red shift of the main peak and the emergence of additional resonance at 510-520 nm (inset in **Figure 2 b**), which is mostly expressed for the 12 nm length but is visible for the 6 nm and 20 nm spike length models. The random and Sobol Au NU models also have a spectral feature at 510-520 nm wavelength, indicating that it is related to the transversal nanorod-like LSPR of the same diameter spikes used throughout the different models. Moreover, the Mie simulations suggest that the dark quadrupolar resonance for the spheres is negligibly smaller and was not observed in the experimental extinction spectra for the Au NSs, [49] but it clearly emerges in the Au NUs (uniform 80|6, 80|12).

There is a big difference between the main resonance of the uniform and different random Au NUs, despite sharing the same size 80 nm core. That indicates the significance of the random spikes, which substantially broadens the LSPR and even a single random spike Au NU depicts the experimental colloidal spectra reasonably because the same tendencies of resonance broadening are met despite differences in core size or spike length (**Figure 2**).

In the case of the uniform spikes, the well-expressed transformation from the dipolar resonance of the sphere to the far red-shifted LSPR emerges only when the aspect ratio of the spikes is over 1. The 50 shortest 6 nm length (L) and 10 nm diameter (D) spikes of 0.6 aspect ratio (L/D) expand the effective diameter of the core only by 1 nm. While the longer 12 nm length and 1.2 aspect ratio spikes or 20 nm length and 2.0 aspect ratio spikes expand the effective diameter of the core to 85 nm and 93 nm, respectively. Simplified Mie-based calculation of the gold sphere in water suggests that only a modest maximum 11.3 nm red-shift of the sphere dipolar resonance from 541.0 nm to 541.7 nm, 545.2 nm, and 552.3 nm should emerge according to the growing effective diameter (Not shown here). Although in practice, as seen in **Figure 2 b,** the modeling suggests an order of magnitude bigger shift of the peak position from the sphere (Au NS 80|0) at 542 nm to the longest spike uniform Au NUs (Au NU 80|20) at 766 nm which is 224 nm. That confirms the significance of the longitudinal nanorod-like LSPR contribution increasing along with the increasing aspect ratio and helps to explain the red-shift of the main resonance with respect to the fixed transversal resonance as was described in earlier Au nanorod studies. [50–52]

To better understand the interaction of the plasmon modes, we took the 80|6, 80|12, and 80|20 nanourchins and excised the tips (80|6, 80|12, 80|20 No cores) and spherical core (80|0) and then modeled the extinction spectrum of each structure. The EM simulation results of uniform spike Au NUs without cores are shown **Figure S6**. The longest tips have peaks at 520 and 579 nm, while the core has a peak at 544 nm. The two plasmon bands of the 80|20 nanourchin can be explained by the nonlinear hybridization of the core (544 nm) and tip (579 nm) dipolar modes to generate a weak plasmon band at 506 nm and a very strong plasmon band at 766 nm (**Figure 3**). [53]

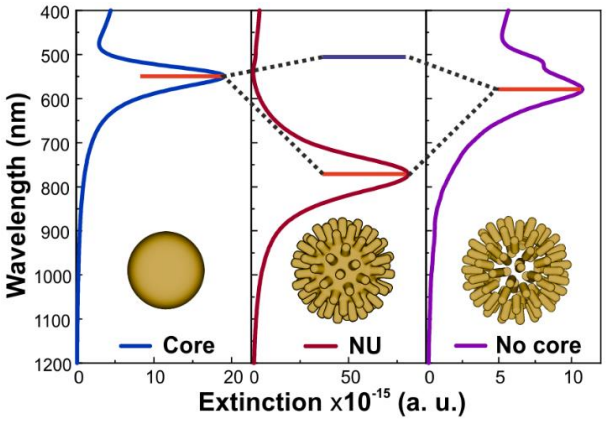


Figure 3. Plasmon hybridization scheme of 80|20 NU sample with a schematic energy-level diagram illustrating the plasmon hybridization mechanism in Au NUs as a result of the interaction between the spherical core and uniformly distributed spike plasmons.

The resonances and their evolution with increasing spike length are even better seen in the near-field calculations depicted in **Figure 4**. The dipolar resonance of the sphere at 542 nm (80|0 nm) shifts to the hybridized dipolar resonance at 577 nm for the 6 nm spike length Au NU (80|6 nm). Polarization maps were extracted by calculating the divergence of the electric field from the simulation data, representing the spatial distribution of induced charge density within the nanourchins under optical excitation. These maps provide insight into the nature and symmetry of the excited plasmonic modes, revealing the interplay between core and spike oscillations and identifying regions of strong local field enhancement. The electron polarization color scale helps to depict the short spike-enhanced quadrupolar resonance at 517 nm, which did not emerge clearly for a pure sphere. The uniformly distributed 12 nm spikes already hinder the core dipolar resonance at 667 nm, and the color map suggests the hybridized longitudinal resonance, while the quadrupole of the sphere at 519 nm is excited along with the transversal resonance in the spikes. The electrical field intensity clearly indicates the field concentration in the uniformly distributed spikes, which is even more expressed when they get longer. The 20 nm spikes demonstrate well-expressed transversal resonances captured at 510 nm and a hybridized longitudinal resonance peaked at 766 nm extending from the opposite sides of the NU. The transversal and longitudinal resonances at the tips are even better seen in the simulations without the core (**Figure S6**). Two absorption bands are commonly observed in Au nanostars [22,28] and nanoflowers [48] with long spikes; therefore, the optical properties modeled for Au NUs and their interpretation show related trends.

The uniform model is easier to interpret but does not fully represent experimental observations, as theoretical resonances appear narrower than experimentally measured spectra. From **Table 1**, we can see that the spike size dispersion can be quite large; therefore, the second absorption peak position might be very broad. Therefore, Sobol and random spike distribution Au NUs were simulated with the same 20 nm average spike length on fixed 80 nm size cores. Their spectrum revealed multiple resonances (**Figure 2 b**), which are depicted in **Figure 4** and **Figure S7**. Despite random spikes, the Au NUs preserve the hybridized transversal spike resonance and quadrupolar dark mode behavior at 510 nm, as the electrical field maps do not indicate field concentration. At longer wavelengths, multiple complex resonances emerge with high field enhancement in the spikes (**Figure S7**).

The simulation findings suggest that by changing the excitation wavelength, one can either target the hybridized quadrupolar mode at 510-520 nm or using longer wavelengths at 570 nm and above, which can excite the hybridized longitudinal modes related to the bright resonances and increase the field concentration in the different length spikes. The resonances at the longer wavelengths are very sensitive to the geometry of spikes.

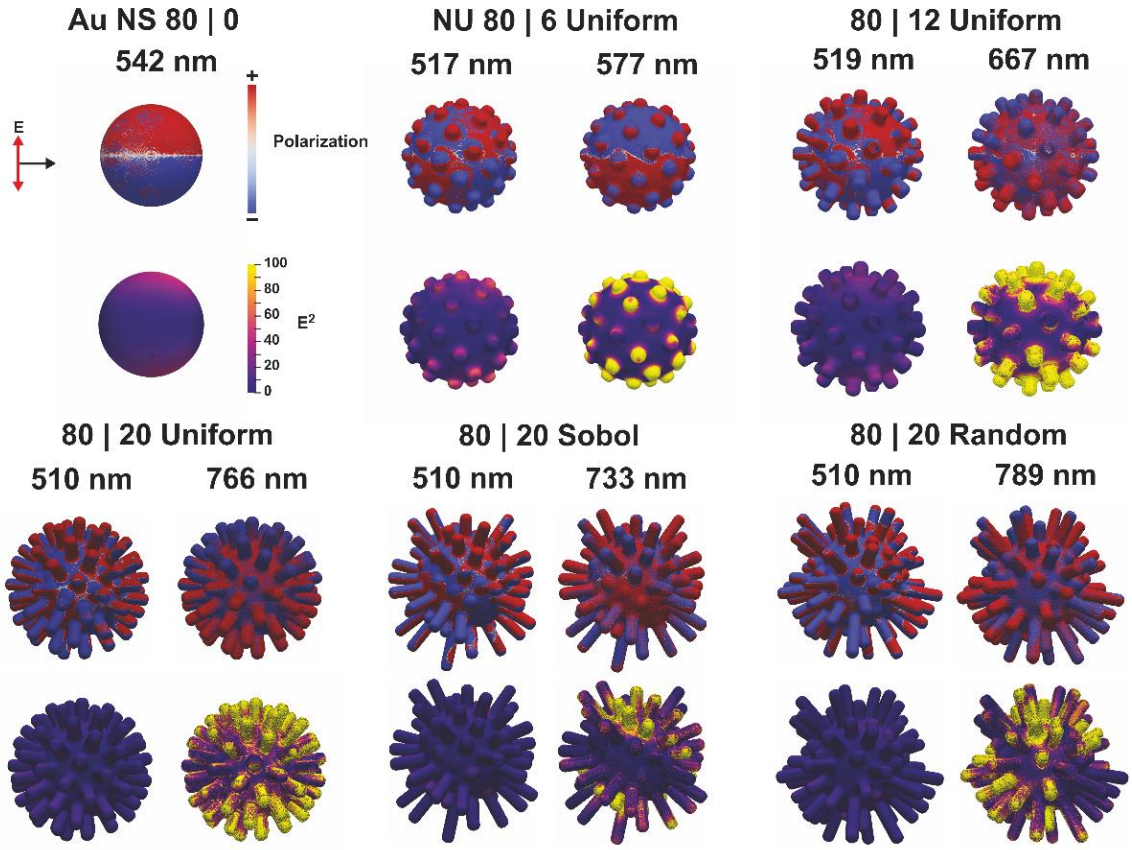


Figure 4. EM simulations of the polarization (above) and electric field distribution (below) for 80 nm diameter gold sphere (Au NS) and nanourchin (Au NU) structures with varying spike lengths at resonant wavelengths indicated above each set of images. The nanourchin core diameter is fixed at 80 nm, with 50 uniformly "Uniform", quasi-random "Sobol", and randomly distributed spikes "Random" having a tip diameter of 10 nm and cylindrical spikes. Spike lengths are 0 nm (sphere), 6 nm, 12 nm, and 20 nm, corresponding to Au NU samples 80|0, 80|6, 80|12, and 80|20, respectively. The color scales represent normalized polarization (top) and electric field intensity (E^2, bottom) for all samples.

Longer and higher aspect ratio Au NUs are carrying multiple resonances ranging from the visible to nIR covering the so-called optical transparency window, or otherwise biological window, which paves the way for numerous optical applications where electrical field concentration can be helpful in optical stimulation, down conversion, sensing, imaging, and other phototherapeutic applications. [54–58]

Transient absorption spectroscopy measurement results of Au nanourchins

Aiming to elucidate the differences in the existing resonances, their spectral, and time dependencies, TAS measurements were carried out for the different core and spike size Au NUs samples summarized in **Table 1** that were excited at a broad range of wavelengths from UV to NIR (350, 500, 600, 700, 750 and 800 nm) aiming to individually excite different nature complex LSPR modes present in Au NUs. The original spectral dependencies and time traces for all investigated samples can be found in the supporting information **Figures S8-S16**. The LSPR decay times were obtained in the range of 1-2 ps, which is characteristic for gold nanostructures [13], meaning that the Ag seeds present in the core do not affect the plasmonic properties of Au NUs significantly. However, a clear dependence on the Au NU linear dimensions on pump wavelength was not observed for electron-phonon (*e-ph*) coupling times. The *e-ph* coupling times of Au NUs are quite similar to Au NSs. Whereas spectral dependencies, especially when normalized at 0 ps delay time to the amplitude of the first negative peak to -1 in the spectra as depicted in **Figure 5** had expressed differences depending on the applied pump wavelengths and length of the Au NU spikes. Short 6-7 nm length spike samples (**Figure 5 d, e, f**) indicated nearly identical TAS spectra despite the used pump wavelength, similar to the Au NS samples of a similar diameter (**Figure 5 a, b, c**) representing the Au NU cores. In contrast, the long spike 12-15 nm Au NUs had a clear difference in the amplitude of the negative TAS signal in the 600-800 nm probe band, depending on the used pump wavelength. The traces excited under $350 \leq \lambda_{pump} \leq 600$ nm had almost 0.5 a.u. difference in the amplitude (indicated by an arrow in **Figure 5 g, h, i**) compared to excited with 700 nm $\leq \lambda_{pump} \leq$ 800 nm. This finding confirms the hypothesis that longer spike lengths in Au NUs lead to a stronger hybridized nanorod-like longitudinal LSPR contribution and broader resonances, as evidenced by both electromagnetic simulations and experimental optical extinction spectra (**Figure 2**). The combined interpretation of the optical simulations and transient absorption measurements further validates the ability to synthesize Au NUs with controlled average spike lengths and to spectrally tune their field enhancements, particularly when spike lengths exceed 10 nm.

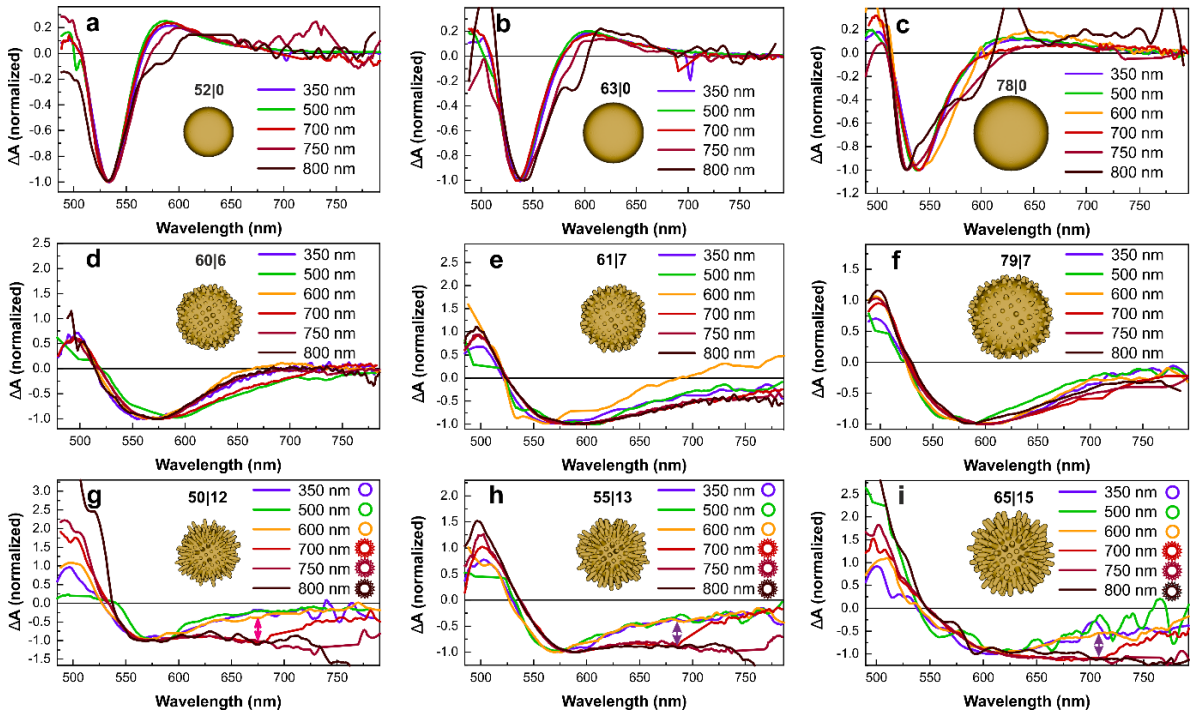


Figure 5. Normalized to -1 negative TAS spectra of samples 52|0 (**a**), 63|0 (**b**), 78|0 (**c**), 60|6 (**d**), 61|7 (**e**), 79|7 (**f**), 50|12 (**g**), 55|13 (**h**), and 65|15 (**i**) at a delay time of 0 ps. The excitation wavelength is depicted in the legend. The vertical double arrow in (**g-i**) indicates the change in TAS spectra at specific excitation. Every figure contains an inset with the representative Au NU model, which is proportional in size.

SERS measurements

Finally, building on the understanding of the resonances in Au NUs, we experimentally evaluated their Raman scattering enhancements by measuring the SERS signals of 78|0 Au NSs, short-spike 79|7 Au NUs, and long-spike 65|15 Au NUs at two excitation wavelengths, 532 nm and 785 nm. SERS measurements were performed using nanoparticle monolayers deposited on silicon substrates and in the liquid phase. The samples were intentionally selected to spectrally separate the core and spike-related resonances, *i.e.*, the NU samples had quite a decent spike aspect ratio difference, *i.e.*, 1 *vs.* 1.5, but still shared a close size of the core, which was almost identical to the NS sample (see insets of **Figure 5 c, f, i**). The investigated nanostructure geometries supported different characteristic LSP resonances stemming firstly from the quadrupolar resonances in the cores, being close to the green excitation wavelength, and shared by both NS and NUs samples. The second, hybridized longitudinal resonance met in the spikes, was characteristic only for the long spike NUs (**Figure 2**, **Figure 3**), being in the nIR wavelength. Both investigated resonances were closely overlapping with the excitation wavelengths typically used for Raman measurements. Validity of the expected resonances was verified carying out the reflectance measurements of the nanostructure layers (**Figure S17**), where one can see that for Au NSs, the reflectance is lower in the shorter wavelength range (400 – 600 nm), whereas for Au NUs, reflectance is even smaller over all spectral range and also depends on the spike length. NUs with long spikes have lower reflectance in 700-1000 nm. This is in agreement with the steady state absorbance measurements in colloids as depicted in **Figure 2 a** as well as in the TAS measurements depicted in **Figure 5**, *i.e.*, the findings support

the presence of the previously discussed LSP resonances. The Au NUs with short spikes spectra somewhat mimic the silicon substrate reflectance, indicating a smaller surface coverage. Variation in layer quality was confirmed from SEM micrographs (**Figure S18**). It was observed that spherical nanoparticles formed a better quality densely packed layer compared to non-continuous deposition for nanourchins' counterparts, which might have impacted the Raman signal enhancement. Therefore, nanoparticle densities were evaluated and used for the enhancement factor (EF) normalization.

The SERS analysis of layers with model 10^{-4} M concentration 2-naphthalene thiol (2NT) molecule (representative Raman scattering spectra of the molecule are shown in **Figure S19** revealed that the highest signal quality was observed for sample 78|0, both excited with 532 nm and 785 nm wavelength (**Figure 6**). This result corresponds well with observations by others if a monolayer of spheres can be treated as aggregated particles. [59] The SERS signal is strongly dependent on the surface structure and material used for the signal enhancement. It was previously shown that different gold structures can be optimized for 633 nm [60] or 785 nm [59] wavelength excitation, but less or no signal enhancement is registered using 532 nm excitation. [59,60] Our results show that we could detect considerable enhancement with 532 nm excitation in the case of spherical particles, but a higher signal was detected with 785 nm excitation, which could confirm the previous observation that gold is showing higher signal enhancement using excitation wavelengths red-shifted from the LSPR peak. [61] Comparing samples, the lower enhancement for the NUs compared to NSs could be partially attributed to the poorer surface packing of NUs. The quality of surface packaging directly corresponds to the hot spot surface density that is responsible for higher signal counts. Moreover, it was reported by D. M. Solís *et al.* [62] that the packing density significantly influences SERS performance. For gold nanospheres and nanorods, SERS efficiency typically increases rapidly with surface coverage above approximately 50%, driven by enhanced hotspot formation in interparticle gaps. However, for highly anisotropic particles like nanostars, which resemble nanourchins, substantial SERS enhancement can occur even in dilute layers and their EF are way less sensitive for the packing density compared to nanospheres. Moreover, very high aggregation densities for such anisotropic particles may not always improve performance and can even be detrimental by forming an effective metamaterial that inhibits hotspot formation in central regions.For the sample 65|15, it was possible to identify four peaks attributable to the 2NT molecule (767 cm^{-1}, 846 cm^{-1}, 1066 cm^{-1}, 1380 cm^{-1}), whereas for the short spike sample, only two peaks (767 cm^{-1}, 1380 cm^{-1}, **Table S2**) were discernible. The excitation with 785 nm resulted in higher intensity and better quality signals from all the samples in general. Longer spike urchins outperformed shorter spike counterparts with at least 2 times higher signal intensity.

We have calculated the signal EF for investigated Au nanostructures employing eq. (S2) [63] by comparing the Raman signal with the one of the 10^{-2} M 2NT molecule measured without nanoparticles (**Figure S19**). Calculated EFs for two peaks at 767 cm^{-1} and 1380 cm^{-1} using 785 nm excitation for 78|0, 79|7, and 65|15 samples are summarized in **Table 2**. It is visible that absolute EF for long spike NUs is *ca*. 6-fold higher than for short spike NUs, which supports the hypothesis that the hybridized LSP resonance and field concentrations in the spikes observed in the EM simulations are contributing as the enhancement factor (**Figure 6** inset). Taking into account the particle densities on the surface, the normalized effective EFs (**Table 2**, S, indicated in parenthesis) were increased but the ratio stayed similar supporting the significance of the spike aspect ratio for the Raman signal enhancement.

The analysis of the SERS signal in liquid phase (**Figure S20**) revealed the same EF tendency (**Table 2**, L) as was observed in case of deposited layers (**Table 2**, S). Despite nanoparticles in liquid are in a "metastable" state due to Brownian motion [64] they still show the same tendency as we observed for the layers. It can be stated that EF tendencies met in Au nanostructure layers on the surface represent well the enhancement effects in volume. This SERS investigation is more of exploratory research rather than an in-depth study, and further experiments would be necessary, but even in the present form, it already signifies the importance of the nanourchins' geometries and especially spike aspect ratio for the electromagnetic enhancement effects and reveals the potential of nanourchins for SERS.

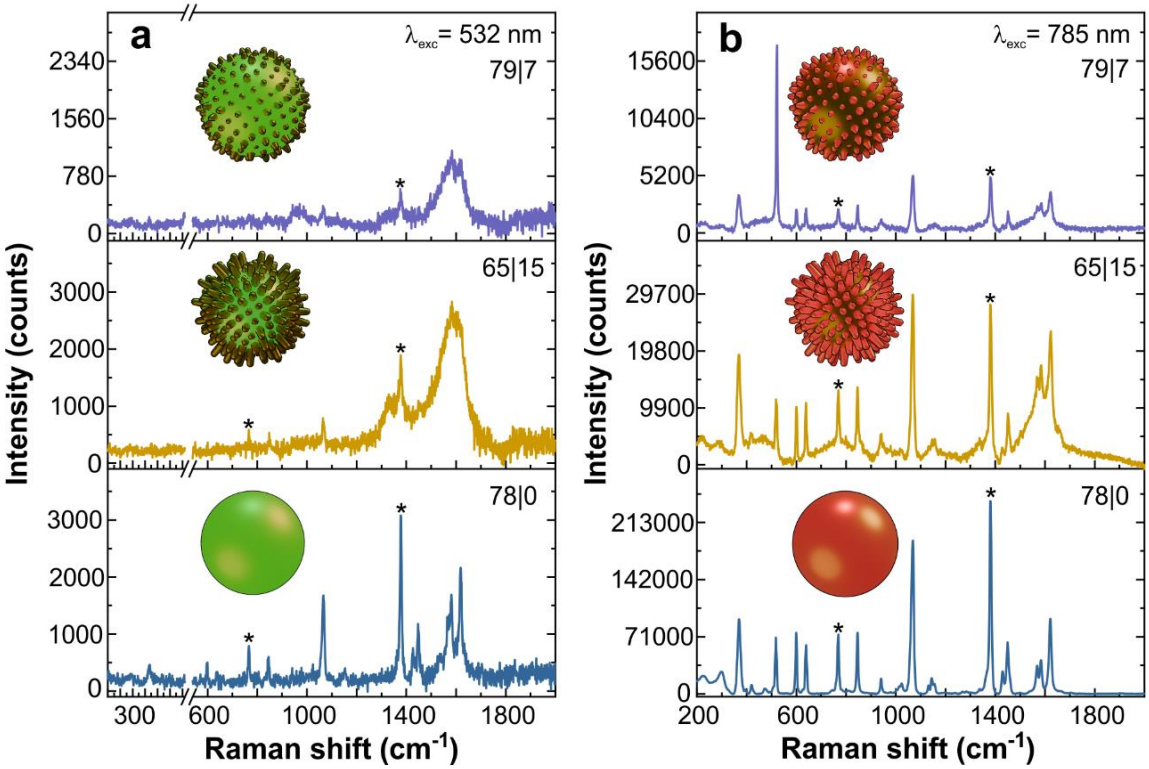


Figure 6. Surface-enhanced Raman-scattering spectroscopy data of Au NP samples 78|0; 79|7, and 65|15 layers on silicon substrate under excitation at 532 nm (**a**) and 785 nm (**b**). The asterisk indicates molecular vibration bands used for the EF analysis. Insets depict a simplified visualization of spike and core resonances characteristic for Au NUs and spheres under different wavelength excitations.

Table 2. SERS enhancement factor (EF) for Au NS and Au NU samples and ratio between short spike and long spike samples ($EF_{65|15}/EF_{79|7}$) for the two characteristic Raman bands identified in **Figure 6**. Measurements were obtained with 785 nm excitation wavelength in solid (S) and liquid (L) state using the same 2NT concentration of 10^{-4} M. For the solid type samples two values are provided, absolute as well as normalized to the nanoparticle density (indicated in parentheses) which was estimated from the analysis of **Figure S17**.

Peak position, cm^{-1}	Sample type	Absolute (Normalized) EF

		78|0	65|15	79|7	Ratio $[EF_{65\|15}/EF_{79\|7}]$
767	S	1.5×10^4	0.27×10^4 (0.68×10^4)	4.1×10^2 (0.14×10^4)	6.6 (4.9)
	L	1.5×10^3	0.29×10^3	0.9×10^2	2.9
1380	S	1.3×10^5	0.16×10^5 (0.41×10^5)	2.8×10^3 (0.1×10^5)	5.7 (4.1)
	L	2.0×10^4	0.28×10^4	0.7×10^3	3.7

Conclusion

The study confirmed that the proposed wet synthesis method is capable of delivering controlled spike length Au NUs, which drives size-dependent hybridized LSPR resonances having strong electrical field enhancements > 600 nm.

The EM simulations suggest that spike lengths tend to override the core dipole moment seen only for ≤ 1 aspect ratio spikes, which are dominated by the hybridized longitudinal resonances typical for nanorods. The transverse resonance of the spikes hybridizes with the quadrupolar resonance of the spherical core.

High aspect ratio Au NU spikes (aspect ratio > 1) deliver strong electric field enhancements concentrated at the spike tips. Uniform Au NU models are good for interpreting the significance of the elongating spikes, but the proposed random Au NUs with the same average spike length delivered much closer spectra to the experimental ones, in spite of the use of a single Au NU in the modeling and size distribution in the colloidal sample.

The time-resolved transient absorption spectroscopy analysis suggested that the applied pump wavelength had a strong effect on the overlap with the spike-related resonances met at 700-800 nm while the LSPR decays did not indicate linear dimension-related dependence, suggesting uniform material qualities.

The wavelength-dependent Raman enhancement of the in-resonance and out-of-resonance Au NUs with different length spikes confirmed the findings in the simulations and TAS, highlighting the significance of spike lengths greater than 10 nm for creating hybridized longitudinal resonances responsible for the strong confinement of the electrical field in the spikes.

This study demonstrates that the plasmonic and optical properties of Au NUs strongly depend on the length and aspect ratio of their spikes, which could be beneficial for practical field enhancement-related applications such as photocatalysis, phototherapy, sensing, and surface-enhanced Raman spectroscopy (SERS).

Supporting Information

3D TEM image of Au NU animation; chemical synthesis of Ag seeds and Au NUs; TEM measurements: Ag seeds, Au NUs TEM images for 3D animation formation; modeling of Au NUs: table of parameters used for modelling, EM simulations of extinction spectra and polarization of Au NUs without cores, EM simulations of Au NU 80|20 Sobol and Random models; transient absorption spectra and traces; reflectance spectra of Au NSs and Au NUs; surface morphology of monolayers used for SERS

analysis; SERS measurements; peaks in the Raman scattering spectrum of the 2NT molecule in powder and dried on surface from solvent; SERS measurements in liquid.

Acknowledgements

The research was implemented within the NANOTRAACES project carried out under the M-ERA.NET 2 scheme. This project has received funding from the Research Council of Lithuania (LMTLT), agreement No MERANET-22–2.

Conflict of Interest

The authors declare no conflict of interest.

Data Availability Statement

The data that support the findings of this study are available from the corresponding author upon reasonable request.

References

(1) Zhang, X.; Chen, Y. L.; Liu, R. S.; Tsai, D. P. Plasmonic Photocatalysis. *Reports Prog. Phys.* **2013**, *76* (4), 046401. https://doi.org/10.1088/0034-4885/76/4/046401.

(2) Kuppe, C.; Rusimova, K. R.; Ohnoutek, L.; Slavov, D.; Valev, V. K. "Hot" in Plasmonics: Temperature-Related Concepts and Applications of Metal Nanostructures. *Adv. Opt. Mater.* **2020**, *8* (1), 1901166. https://doi.org/10.1002/adom.201901166.

(3) Ellis, M. G.; Pant, U.; Lou-Franco, J.; Logan, N.; Cao, C. Directed Assembly of Au Nanostar@Ag Satellite Nanostructures for SERS-Based Sensing of Hg 2+ Ions. *ACS Appl. Nano Mater.* **2023**, *6* (12), 10431–10440. https://doi.org/10.1021/acsanm.3c01382.

(4) Kim, W.; Kim, N.; Park, J. W.; Kim, Z. H. Nanostar Probes for Tip-Enhanced Spectroscopy. *Nanoscale* **2016**, *8* (2), 987–994. https://doi.org/10.1039/c5nr06657c.

(5) Liu, Y.; Yuan, H.; Kersey, F. R.; Register, J. K.; Parrott, M. C.; Vo-Dinh, T. Plasmonic Gold Nanostars for Multi-Modality Sensing and Diagnostics. *Sensors (Switzerland)* **2015**, *15* (2), 3706–3720. https://doi.org/10.3390/s150203706.

(6) Reineck, P.; Lee, G. P.; Brick, D.; Karg, M.; Mulvaney, P.; Bach, U. A Solid-State Plasmonic Solar Cell via Metal Nanoparticle Self-Assembly. *Adv. Mater.* **2012**, *24* (35), 4750–4755. https://doi.org/10.1002/adma.201200994.

(7) Liu, Y.; Ye, H.; Bayram, A.; Zhang, T.; Cai, Q.; Xie, C.; Huynh, H. D.; Peerzade, S. A. M. A.; Kahn, J. S.; Qin, Z. Gold Nanourchins Improve Virus Targeting and Plasmonic Coupling for Virus Diagnosis on a Smartphone Platform. *ACS Sensors* **2022**, *7* (12), 3741–3752. https://doi.org/10.1021/acssensors.2c01552.

(8) Samhadaneh, D. M.; Chu, S.; Maysinger, D.; Stochaj, U. How Could Gold Nanourchins Be Applied in the Clinic? *Nanomedicine* **2020**, *15* (9), 829–832.

https://doi.org/10.2217/nnm-2019-0438.

(9) Pakravan, A.; Salehi, R.; Mahkam, M. Comparison Study on the Effect of Gold Nanoparticles Shape in the Forms of Star, Hallow, Cage, Rods, and Si-Au and Fe-Au Core-Shell on Photothermal Cancer Treatment. *Photodiagnosis Photodyn. Ther.* **2021**, *33*, 102144. https://doi.org/10.1016/j.pdpdt.2020.102144.

(10) Kim, J. H.; Jeon, S.; In, J. H.; Nam, S.; Jin, H. M.; Han, K. H.; Yang, G. G.; Choi, H. J.; Kim, K. M.; Shin, J.; Son, S. W.; Kwon, S. J.; Kim, B. H.; Kim, S. O. Publisher Correction: Nanoscale Physical Unclonable Function Labels Based on Block Copolymer Self-Assembly. *Nat. Electron.* **2022**, *5* (8), 539–539. https://doi.org/10.1038/s41928-022-00829-4.

(11) Yang, G. G.; Choi, H. J.; Li, S.; Kim, J. H.; Kwon, K.; Jin, H. M.; Kim, B. H.; Kim, S. O. Intelligent Block Copolymer Self-Assembly towards IoT Hardware Components. *Nat. Rev. Electr. Eng.* **2024**, *1* (2), 124–138. https://doi.org/10.1038/s44287-024-00017-w.

(12) Liu, X. Colloidal Plasmonic Nanoparticles for Ultrafast Optical Switching and Laser Pulse Generation. *Front. Mater.* **2018**, *5* (September), 1–7. https://doi.org/10.3389/fmats.2018.00059.

(13) Peckus, D.; Tamuleviciene, A.; Mougin, K.; Spangenberg, A.; Vidal, L.; Bauerlin, Q.; Keller, M.; Henzie, J.; Puodziukynas, L.; Tamulevicius, T.; Tamulevicius, S. Shape Influence on the Ultrafast Plasmonic Properties of Gold Nanoparticles. *Opt. Express* **2022**, *30* (15), 27730–27745. https://doi.org/10.1364/oe.463961.

(14) Khinevich, N.; Peckus, D.; Tamulevičienė, A.; Klimaitė, G.; Henzie, J.; Tamulevičius, T.; Tamulevičius, S. Size and Crystallinity Effect on the Ultrafast Optical Response of Chemically Synthesized Silver Nanoparticles. *J. Mater.* **2024**, *10* (3), 594–600. https://doi.org/10.1016/j.jmat.2023.08.009.

(15) Issaad, D.; Moustaoui, H.; Medjahed, A.; Lalaoui, L.; Spadavecchia, J.; Bouafia, M.; De La Chapelle, M. L.; Djaker, N. Scattering Correlation Spectroscopy and Raman Spectroscopy of Thiophenol on Gold Nanoparticles: Comparative Study between Nanospheres and Nanourchins. *J. Phys. Chem. C* **2017**, *121* (33), 18254–18262. https://doi.org/10.1021/acs.jpcc.7b05355.

(16) Liang, X.; Zhang, H.; Xu, C.; Cao, D.; Gao, Q.; Cheng, S. Condensation Effect-Induced Improved Sensitivity for SERS Trace Detection on a Superhydrophobic Plasmonic Nanofibrous Mat. *RSC Adv.* **2017**, *7* (70), 44492–44498. https://doi.org/10.1039/c7ra09194j.

(17) Pazos-Perez, N.; Guerrini, L.; Alvarez-Puebla, R. A. Plasmon Tunability of Gold Nanostars at the Tip Apexes. *ACS Omega* **2018**, *3* (12), 17173–17179. https://doi.org/10.1021/acsomega.8b02686.

(18) Chatterjee, S.; Ringane, A. B.; Arya, A.; Das, G. M.; Dantham, V. R.; Laha, R.; Hussian, S. A High-Yield, One-Step Synthesis of Surfactant-Free Gold Nanostars and Numerical Study for Single-Molecule SERS Application. *J. Nanoparticle Res.* **2016**, *18* (8), 1–9. https://doi.org/10.1007/s11051-016-3557-0.

(19) Ba, J.; Han, Y.; Zhang, X.; Zhang, L.; Hui, S.; Huang, Z.; Yang, W. Au Nanoflowers for Catalyzing and in Situ Surface-Enhanced Raman Spectroscopy Monitoring of the Dimerization of p-Aminothiophenol. *ACS Omega* **2021**, *6* (39), 25720–25728.

https://doi.org/10.1021/acsomega.1c03933.

(20) Seo, M.; Ha, J. W. Effective Surface-Enhanced Raman Scattering of Randomly Branched Gold Nano-Urchins with Rhodamine 6G as Raman Reporters. *Microchem. J.* **2018**, *140*, 47–51. https://doi.org/10.1016/j.microc.2018.04.004.

(21) Tran, N. T.; Nguyen, T. G.; Le, M. T.; Trinh, K. S.; Phung, V. D.; Huynh, A. T. N.; Pham, N. T. Highly Branched and Hollow Gold Nanourchins for Bacterial Killing and Off-Resonance SERS Sensing. *Chem. Pap.* **2023**, *77* (12), 7505–7514. https://doi.org/10.1007/s11696-023-03077-8.

(22) Becerril-Castro, I. B.; Calderon, I.; Pazos-Perez, N.; Guerrini, L.; Schulz, F.; Feliu, N.; Chakraborty, I.; Giannini, V.; Parak, W. J.; Alvarez-Puebla, R. A. Gold Nanostars: Synthesis, Optical and SERS Analytical Properties. *Anal. Sens.* **2022**, *2* (3). https://doi.org/10.1002/anse.202200005.

(23) Riswana Barveen, N.; Wang, T.-J.; Chang, Y.-H. Photochemical Synthesis of Au Nanostars on PMMA Films by Ethanol Action as Flexible SERS Substrates for In-Situ Detection of Antibiotics on Curved Surfaces. *Chem. Eng. J.* **2022**, *431*, 134240. https://doi.org/https://doi.org/10.1016/j.cej.2021.134240.

(24) Niu, W.; Chua, Y. A. A.; Zhang, W.; Huang, H.; Lu, X. Highly Symmetric Gold Nanostars: Crystallographic Control and Surface-Enhanced Raman Scattering Property. *J. Am. Chem. Soc.* **2015**, *137* (33), 10460–10463. https://doi.org/10.1021/jacs.5b05321.

(25) Zhao, Y. X.; Kang, H. Sen; Zhao, W. Q.; Chen, Y. L.; Ma, L.; Ding, S. J.; Chen, X. B.; Wang, Q. Q. Dual Plasmon Resonances and Tunable Electric Field in Structure-Adjustable Au Nanoflowers for Improved Sers and Photocatalysis. *Nanomaterials* **2021**, *11* (9), 0–10. https://doi.org/10.3390/nano11092176.

(26) Kariuki, V. M.; Hoffmeier, J. C.; Yazgan, I.; Sadik, O. A. Seedless Synthesis and SERS Characterization of Multi-Branched Gold Nanoflowers Using Water Soluble Polymers. *Nanoscale* **2017**, *9* (24), 8330–8340. https://doi.org/10.1039/c7nr01233k.

(27) Atta, S.; Tsoulos, T. V.; Fabris, L. Shaping Gold Nanostar Electric Fields for Surface-Enhanced Raman Spectroscopy Enhancement via Silica Coating and Selective Etching. *J. Phys. Chem. C* **2016**, *120* (37), 20749–20758. https://doi.org/10.1021/acs.jpcc.6b01949.

(28) Nehl, C. L.; Liao, H.; Hafner, J. H. Optical Properties of Star-Shaped Gold Nanoparticles. *Nano Lett.* **2006**, *6* (4), 683–688. https://doi.org/10.1021/nl052409y.

(29) Siegel, A. L.; Baker, G. A. Bespoke Nanostars: Synthetic Strategies, Tactics, and Uses of Tailored Branched Gold Nanoparticles. *Nanoscale Adv.* **2021**, *3* (14), 3980–4004. https://doi.org/10.1039/D0NA01057J.

(30) Xu, F.; Cui, K.; Sun, Y.; Guo, C.; Liu, Z.; Zhang, Y.; Shi, Y.; Li, Z. Facile Synthesis of Urchin-like Gold Submicrostructures for Nonenzymatic Glucose Sensing. *Talanta* **2010**, *82* (5), 1845–1852. https://doi.org/10.1016/j.talanta.2010.07.087.

(31) Bastús, N. G.; Merkoçi, F.; Piella, J.; Puntes, V. Synthesis of Highly Monodisperse Citrate-Stabilized Silver Nanoparticles of up to 200 Nm: Kinetic Control and Catalytic Properties. *Chem. Mater.* **2014**, *26* (9), 2836–2846. https://doi.org/10.1021/cm500316k.

(32) Lee, S. H.; Jun, B. H. Silver Nanoparticles: Synthesis and Application for Nanomedicine. *Int. J. Mol. Sci.* **2019**, *20* (4). https://doi.org/10.3390/ijms20040865.

(33) Dzimitrowicz, A.; Jamróz, P.; DiCenzo, G. C.; Sergiel, I.; Kozlecki, T.; Pohl, P. Preparation and Characterization of Gold Nanoparticles Prepared with Aqueous Extracts of Lamiaceae Plants and the Effect of Follow-up Treatment with Atmospheric Pressure Glow Microdischarge. *Arab. J. Chem.* **2019**, *12* (8), 4118–4130. https://doi.org/10.1016/j.arabjc.2016.04.004.

(34) Amendola, V.; Meneghetti, M. Size Evaluation of Gold Nanoparticles by UV-Vis Spectroscopy. *J. Phys. Chem. C* **2009**, *113* (11), 4277–4285. https://doi.org/10.1021/jp8082425.

(35) De Silva Indrasekara, A. S.; Johnson, S. F.; Odion, R. A.; Vo-Dinh, T. Manipulation of the Geometry and Modulation of the Optical Response of Surfactant-Free Gold Nanostars: A Systematic Bottom-Up Synthesis. *ACS Omega* **2018**, *3* (2), 2202–2210. https://doi.org/10.1021/acsomega.7b01700.

(36) Klinavičius, T.; Khinevich, N.; Tamulevičienė, A.; Vidal, L.; Tamulevičius, S.; Tamulevičius, T. Deep Learning Methods for Colloidal Silver Nanoparticle Concentration and Size Distribution Determination from UV-Vis Extinction Spectra. *J. Phys. Chem. C* **2024**, *128* (23), 9662–9675. https://doi.org/10.1021/acs.jpcc.4c02459.

(37) Kedawat, G.; Sharma, I.; Nagpal, K.; Kumar, M.; Gupta, G.; Gupta, B. K. Studies of Ultrafast Transient Absorption Spectroscopy of Gold Nanorods in an Aqueous Solution. *ACS Omega* **2019**, *4* (7), 12626–12631. https://doi.org/10.1021/acsomega.9b01157.

(38) Ortolani, M.; Mancini, A.; Budweg, A.; Garoli, D.; Brida, D.; de Angelis, F. Pump-Probe Spectroscopy Study of Ultrafast Temperature Dynamics in Nanoporous Gold. *Phys. Rev. B* **2019**, 1–6.

(39) Peckus, D.; Chauvin, A.; Tamulevičius, T.; Juodėnas, M.; Ding, J.; Choi, C.-H.; Mel, A.-A. El; Tessier, P.-Y.; Tamulevičius, S. Polarization Dependent Ultrafast Plasmon Relaxation Dynamics in Nanoporous Gold Thin Films and Nanowires. *J. Phys. D. Appl. Phys.* **2019**, *52*, 225103. https://doi.org/10.1088/1361-6463/ab0719.

(40) Bastús, N. G.; Comenge, J.; Puntes, V. Kinetically Controlled Seeded Growth Synthesis of Citrate-Stabilized Gold Nanoparticles of up to 200 Nm: Size Focusing versus Ostwald Ripening. *Langmuir* **2011**, *27* (17), 11098–11105. https://doi.org/10.1021/la201938u.

(41) Silvestri, A.; Lay, L.; Psaro, R.; Polito, L.; Evangelisti, C. Fluidic Manufacture of Star-Shaped Gold Nanoparticles. *Chem. – A Eur. J.* **2017**, *23* (41), 9732–9735. https://doi.org/10.1002/chem.201701617.

(42) Sun, Z.; Umar, A.; Zeng, J.; Luo, X.; Song, L.; Zhang, Z.; Chen, Z.; Li, J.; Su, F.; Huang, Y. Highly Pure Gold Nanotriangles with Almost 100% Yield for Surface-Enhanced Raman Scattering. *ACS Appl. Nano Mater.* **2022**, *5* (1), 1220–1231. https://doi.org/10.1021/acsanm.1c03827.

(43) Shen, Z.; Sun, J.; Wang, Y.; He, X.; Bao, H.; Zhou, X. Semi-Dense Feature Matching With Transformers and Its Applications in Multiple-View Geometry. *IEEE Trans. Pattern Anal. Mach. Intell.* **2023**, *45* (6), 7726–7738. https://doi.org/10.1109/TPAMI.2022.3223530.

(44) McPeak, K. M.; Jayanti, S. V.; Kress, S. J. P.; Meyer, S.; Iotti, S.; Rossinelli, A.; Norris, D. J. Plasmonic Films Can Easily Be Better: Rules and Recipes. *ACS Photonics* **2015**, *2* (3), 326–333. https://doi.org/10.1021/ph5004237.

(45) Joe, S.; Kuo, F. Y. Constructing Sobol Sequences with Better Two-Dimensional Projections. *SIAM J. Sci. Comput.* **2008**, *30* (5), 2635–2654. https://doi.org/10.1137/070709359.

(46) Atanassov, E.; Ivanovska, S.; Karaivanova, A. Optimization of the Direction Numbers of the Sobol Sequences. In *Advances in High Performance Computing*; Dimov, I., Fidanova, S., Eds.; Springer International Publishing: Cham, 2021; pp 145–154.

(47) Kim, G. W.; Ha, J. W. Direct Visualization of Wavelength-Dependent Single Dipoles Generated on Single Gold Nanourchins with Sharp Branches. *Nanoscale Res. Lett.* **2018**, *13*, 0–6. https://doi.org/10.1186/s11671-018-2675-2.

(48) Liu, S.; Zhang, J.; Yan, W. Controllable Synthesis of Three-Dimensional Chiral Au Nanoflowers Induced by Cysteine with Excellent Biocompatible Properties. *Nanomaterials* **2024**, *14* (24). https://doi.org/10.3390/nano14242040.

(49) Rodríguez-Fernández, J.; Pérez-Juste, J.; García De Abajo, F. J.; Liz-Marzán, L. M. Seeded Growth of Submicron Au Colloids with Quadrupole Plasmon Resonance Modes. *Langmuir* **2006**, *22* (16), 7007–7010. https://doi.org/10.1021/la060990n.

(50) Wang, D.-S.; Hsu, F.-Y.; Lin, C.-W. Surface Plasmon Effects on Two Photon Luminescence of Gold Nanorods. *Opt. Express* **2009**, *17* (14), 11350. https://doi.org/10.1364/oe.17.011350.

(51) Ni, W.; Kou, X.; Yang, Z.; Wang, J. Tailoring Longitudinal Surface Plasmon Wavelengths, Scattering and Absorption Cross Sections of Gold Nanorods. *ACS Nano* **2008**, *2* (4), 677–686. https://doi.org/10.1021/nn7003603.

(52) He, G. S.; Zhu, J.; Yong, K.-T.; Baev, A.; Cai, H.-X.; Hu, R.; Cui, Y.; Zhang, X.-H.; Prasad, P. N. Scattering and Absorption Cross-Section Spectral Measurements of Gold Nanorods in Water. *J. Phys. Chem. C* **2010**, *114* (7), 2853–2860. https://doi.org/10.1021/jp907811g.

(53) Prodan, E.; Radloff, C.; Halas, N. J.; Nordlander, P. A Hybridization Model for the Plasmon Response of Complex Nanostructures. *Science (80-.).* **2003**, *302* (5644), 419–422. https://doi.org/10.1126/science.1089171.

(54) Vickerman, B. M.; Zywot, E. M.; Tarrant, T. K.; Lawrence, D. S. Taking Phototherapeutics from Concept to Clinical Launch. *Nat. Rev. Chem.* **2021**, *5* (11), 816–834. https://doi.org/10.1038/s41570-021-00326-w.

(55) Chelushkin, P. S.; Shakirova, J. R.; Kritchenkov, I. S.; Baigildin, V. A.; Tunik, S. P. Phosphorescent NIR Emitters for Biomedicine: Applications{,} Advances and Challenges. *Dalt. Trans.* **2022**, *51* (4), 1257–1280. https://doi.org/10.1039/D1DT03077A.

(56) Hauck, T. S.; Chan, W. C. W. Gold Nanoshells in Cancer Imaging and Therapy: Towards Clinical Application. *Nanomedicine* **2007**, *2* (5), 735–738. https://doi.org/10.2217/17435889.2.5.735.

(57) Zhong, Y.; Dai, H. A Mini-Review on Rare-Earth down-Conversion Nanoparticles for NIR-II Imaging of Biological Systems. *Nano Res.* **2020**, *13* (5), 1281–1294. https://doi.org/10.1007/s12274-020-2721-0.

(58) Lee, E. S.; Lee, J.; Kim, J.; Kim, J.; Wi, J. S.; Park, J. Y.; Lee, T. G.; Choi, B. G.; Lee, K. G.; Kim, Y. H.; Kim, C.; Na, H. K. Janus Gold Nanodiscs with an Asymmetrically

Positioned Polyaniline Nano-Urchin for Photothermal Therapy and Multimodal Imaging in the Second Near-Infrared Window. *ACS Appl. Mater. Interfaces* **2025**, *17* (22), 31799–31809. https://doi.org/10.1021/acsami.4c22576.

(59) Tian, F.; Bonnier, F.; Casey, A.; Shanahan, A. E.; Byrne, H. J. Surface Enhanced Raman Scattering with Gold Nanoparticles: Effect of Particle Shape. *Anal. Methods* **2014**, *6* (22), 9116–9123. https://doi.org/10.1039/C4AY02112F.

(60) Yoo, S.; Park, J.; Nam, D. H.; Kim, S.; Jeong, D.; Lee, M.-K.; Lee, S. Highly Sensitive SERS-Active Substrate with Uniform Gold Nanostructures on Heat-Treated Ni Foam for Detection of Cardiovascular Disease Biomarker. *Nanoscale Adv.* **2025**, *7* (8), 2171–2181. https://doi.org/10.1039/D5NA00052A.

(61) Álvarez-Puebla, R. A. Effects of the Excitation Wavelength on the SERS Spectrum. *J. Phys. Chem. Lett.* **2012**, *3* (7), 857–866. https://doi.org/10.1021/jz201625j.

(62) Solís, D. M.; Taboada, J. M.; Obelleiro, F.; Liz-Marzán, L. M.; García De Abajo, F. J. Optimization of Nanoparticle-Based SERS Substrates through Large-Scale Realistic Simulations. *ACS Photonics* **2017**, *4* (2), 329–337. https://doi.org/10.1021/acsphotonics.6b00786.

(63) Mikalkevičius, M.; Khinevich, N.; Tamulevičius, S.; Tamulevičius, T.; Tamulevičienė, A. Templated Silver Nanoparticle Deposition on Laser-Induced Periodic Surface Structures for SERS Sensing. *Surfaces and Interfaces* **2024**, *51*, 104603. https://doi.org/https://doi.org/10.1016/j.surfin.2024.104603.

(64) Langer, J.; Jimenez de Aberasturi, D.; Aizpurua, J.; Alvarez-Puebla, R. A.; Auguié, B.; Baumberg, J. J.; Bazan, G. C.; Bell, S. E. J.; Boisen, A.; Brolo, A. G.; Choo, J.; Cialla-May, D.; Deckert, V.; Fabris, L.; Faulds, K.; García de Abajo, F. J.; Goodacre, R.; Graham, D.; Haes, A. J.; Haynes, C. L.; Huck, C.; Itoh, T.; Käll, M.; Kneipp, J.; Kotov, N. A.; Kuang, H.; Le Ru, E. C.; Lee, H. K.; Li, J.-F.; Ling, X. Y.; Maier, S. A.; Mayerhöfer, T.; Moskovits, M.; Murakoshi, K.; Nam, J.-M.; Nie, S.; Ozaki, Y.; Pastoriza-Santos, I.; Perez-Juste, J.; Popp, J.; Pucci, A.; Reich, S.; Ren, B.; Schatz, G. C.; Shegai, T.; Schlücker, S.; Tay, L.-L.; Thomas, K. G.; Tian, Z.-Q.; Van Duyne, R. P.; Vo-Dinh, T.; Wang, Y.; Willets, K. A.; Xu, C.; Xu, H.; Xu, Y.; Yamamoto, Y. S.; Zhao, B.; Liz-Marzán, L. M. Present and Future of Surface-Enhanced Raman Scattering. *ACS Nano* **2020**, *14* (1), 28–117. https://doi.org/10.1021/acsnano.9b04224.

Table of Contents (TOC)

